Dynamos in precessing cubes

2016 New J. Phys. 18 103019

(http://iopscience.iop.org/1367-2630/18/10/103019)

IOP Publishing New J. Phys. 18 (2016) 103019 doi:10.1088/1367-2630/18/10/103019

New Journal of Physics
The open access journal at the forefront of physics

Deutsche Physikalische Gesellschaft DPG
IOP Institute of Physics

Published in partnership with: Deutsche Physikalische Gesellschaft and the Institute of Physics

OPEN ACCESS

RECEIVED
6 June 2016

REVISED
2 August 2016

ACCEPTED FOR PUBLICATION
15 August 2016

PUBLISHED
13 October 2016

PAPER

Dynamos in precessing cubes

O Goepfert and A Tilgner[1]

Institute of Geophysics, University of Göttingen, Friedrich-Hund-Platz 1, D-37077 Göttingen, Germany
[1] Author to whom any correspondence should be addressed.

E-mail: andreas.tilgner@phys.uni-goettingen.de

Keywords: magnetohydrodynamics, dynamos, rotating fluids

Abstract

We investigate with numerical simulations the dynamo properties of liquid flows in precessing cubes. There are some similarities with the flow in precessing spheres. Instabilities in the form of triad resonances are observed. The flow is turbulent far above the onset of instability but simplifies to a single vortex for certain control parameters. The critical magnetic Reynolds numbers for the onset of magnetic field generation are lower than, but comparable to, the numbers known for precessing spheres, and are larger than the Reynolds numbers realizable in an experiment currently under construction in Dresden.

1. Introduction

The dynamo mechanism is generally believed to be responsible for the generation of magnetic fields in planets and stars. In this scenario, the kinetic energy of the motion of an electrically conducting fluid is transformed into magnetic energy. It is frequently assumed that thermal or chemical buoyancy supplies the motion of the fluid with energy, but mechanical energy injection is possible, too. Precession driven motion was demonstrated numerically to allow for dynamo action in spheres [1, 2], ellipsoids [3], plane layers [4] and cylinders [5], and tidally [6], libration [7] and collision driven dynamos [8] exist, too.

The study of convection driven dynamos is far more advanced than the investigation of mechanically forced dynamos. This is partly due to the fact that numerical simulations of convective dynamos are less demanding. It is a reasonable model to study these dynamos for example in spherical shells with stress free boundaries, thus avoiding the need to resolve Ekman boundary layers. Precession on the contrary is unable to maintain a stationary state with a non-trivial motion in a liquid filled container with stress free boundaries rotating about an axis of symmetry [9]. Previous simulations of precession driven flows either made the effort to resolve the boundary layers on no slip boundaries, or simulated transients [9], or introduced special boundary conditions [3]. In non-axisymmetric containers, pressure forces exerted by the walls are potentially able to drive a flow which leads to dynamo action, so that no viscous coupling to walls and no slip boundaries are necessary.

The rationale of the present paper is to find a system which allows to investigate precession dynamos in laminar and if possible turbulent states with minimal numerical effort, which means chiefly with stress free boundaries. We chose a cube as non-axisymmetric container because it allows us to discretize space on a Cartesian grid. Precessing cubes have been studied once before [10], but in a parameter regime in which the existence of dynamos is at doubt. A cube is of course not an astrophysically relevant geometry, but one may naively expect the flow in a cube to resemble the flow in the largest sphere enclosed by the cube with dead water in the corners. At any rate, there are some features common to precessing flows in all geometries, such as the appearance of triad resonances, so that any geometry is useful as a model system. Apart from geophysics and astrophysics, there is also an interest in precession for laboratory dynamo experiments dating back to Gans [11] and which is currently revived [12, 13]. The main challenge for a laboratory experiment is to build an apparatus capable of sustaining any magnetic field at all. It is not realistic to build a spherical precessing dynamo based on the numbers in [1], but one may hope that the corners of a cube lead to a more efficient stirring of the fluid and better dynamos. We already have examples of dynamos in which rough boundaries or boundaries with some complexity are preferred over smooth boundaries. The VKS experiment [14] drives liquid sodium with two

rotating disks with blades attached to them, because smooth disks without blades do not provide enough energy input. Spherical Couette flow is a dynamo, and it is predicted that rough spherical boundaries are helpful in this case [15]. The application to laboratory experiments is the main motivation for the study presented here.

The next section presents the mathematical formulation of the problem and the numerical methods used to solve the equations. The subsequent sections will study in turn the laminar flow, its hydrodynamic instability, and the kinematic dynamo effect.

2. Mathematical model and numerical methods

Consider a cube of side length L filled with incompressible liquid of density ρ and viscosity ν, rotating with angular frequency $\tilde{\omega}_D$ about the x-axis and precessing with angular frequency $\tilde{\Omega}_P$. The x-axis is part of a Cartesian tripod attached to the cube, whose sides are parallel to x, y and z-axes. The index D in $\tilde{\omega}_D$ stands for diurnal rotation, a term borrowed from the geophysical application [16]. The precession axis forms the angle α with the x-axis.

In order to remove dimensions form the equation of motion, we choose L as unit of length and the inverse of the total rotation frequency about the x-axis as unit of time. This is approximately $1/\tilde{\omega}_D$ in astrophysical applications because $\tilde{\omega}_D \gg \tilde{\Omega}_P$, but in laboratory experiments, $\tilde{\omega}_D$ and $\tilde{\Omega}_P$ can be comparable, so that we take $1/(\tilde{\omega}_D + \tilde{\Omega}_P \cos\alpha)$ as unit of time. $\tilde{\omega}_D$ and $\tilde{\Omega}_P$ in an experiment are the rotation rate of a motor mounted on the x-axis of the cube and the rotation rate of a turntable precessing the x-axis in inertial space, respectively. Their non-dimensional counterparts ω_D and Ω_P are:

$$\omega_D = \frac{\tilde{\omega}_D}{\tilde{\omega}_D + \tilde{\Omega}_P \cos\alpha} = \frac{1}{1 + \Omega \cos\alpha}, \tag{1}$$

$$\Omega_P = \frac{\tilde{\Omega}_P}{\tilde{\omega}_D + \tilde{\Omega}_P \cos\alpha} = \frac{\Omega}{1 + \Omega \cos\alpha} \tag{2}$$

with $\Omega = \Omega_P/\omega_D = \tilde{\Omega}_P/\tilde{\omega}_D$. Let hats denote unit vectors. In the x, y, z-frame, which we will call the 'boundary frame' from now on, the vector of precession $\boldsymbol{\Omega}_P$ is given by

$$\boldsymbol{\Omega}_P = \Omega_P \cos\alpha\, \hat{\boldsymbol{x}} + \Omega_P\, \boldsymbol{p}(t) \tag{3}$$

with

$$\boldsymbol{p}(t) = \sin\alpha(\cos\omega_D t\, \hat{\boldsymbol{y}} - \sin\omega_D t\, \hat{\boldsymbol{z}}). \tag{4}$$

The equation of motion for the (non-dimensional) velocity $\boldsymbol{v}(\boldsymbol{r}, t)$ as a function of position $\boldsymbol{r}$ and time t and the pressure $p(\boldsymbol{r}, t)$ reads in the frame attached to the cube

$$\begin{aligned} &\partial_t \boldsymbol{v} + (\boldsymbol{v}\cdot\nabla)\boldsymbol{v} + 2(\hat{\boldsymbol{x}} + \Omega_P \boldsymbol{p}(t)) \times \boldsymbol{v} \\ &\quad = -\nabla p + \mathrm{Ek}\nabla^2\boldsymbol{v} + \Omega_P\omega_D(\hat{\boldsymbol{x}} \times \boldsymbol{p}(t)) \times \boldsymbol{r} \end{aligned} \tag{5}$$

$$\nabla\cdot\boldsymbol{v} = 0 \tag{6}$$

with an Ekman number Ek given by

$$\mathrm{Ek} = \frac{\nu}{(\tilde{\omega}_D + \tilde{\Omega}_P\cos\alpha)L^2}. \tag{7}$$

An alternative option is to formulate the problem in the 'precession frame' [16], which is chosen such that the precession and rotation axes are stationary, which implies that this frame is rotating about the precession axis when viewed from inertial space. The precession frame is of interest here because it reveals the role of non-axisymmetric containers [9]. In the precession frame, the boundaries rotate about the x-axis but are stationary otherwise. Suppose the container is symmetric about this axis, so that the shape of the boundaries does not change in the course of time in the precession frame. The work done by pressure forces, $\oint p\boldsymbol{v}\cdot\hat{\boldsymbol{n}}\mathrm{d}A$, where $\hat{\boldsymbol{n}}$ is a unit normal vector to the boundary and the integral extends over the entire boundary, is then zero because $\boldsymbol{v}\cdot\hat{\boldsymbol{n}} = 0$ on the boundary. If in addition the boundaries are stress free, there is nothing left to drive a flow. Every motion must come to rest with the exception of a solid body rotation in spherical boundaries because this motion does not dissipate in the bulk and can go on for ever within stress free boundaries. However, a solid body rotation cannot support a dynamo. We conclude that if we are looking for a precession driven dynamo with stress free boundaries, we will not find any in containers rotating about an axis of symmetry.

If we opt for a cube as non-axisymmetric container, the precession frame is unpleasant to use because of the moving boundaries and we return to the boundary frame and equations (5) and (6). A convenient method for solving these equations is a finite difference method implemented on GPUs. This method was already used for the simulation of convection driven dynamos [17, 18]. Its main feature is to replace a strictly incompressible fluid by a weakly compressible one in order to avoid the need for a Poisson solver running on GPUs [18]. This

method introduces a sound speed c, replaces $\nabla \cdot \boldsymbol{v} = 0$ with a linearized continuity equation $\partial_t \rho + \nabla \cdot \boldsymbol{v} = 0$ and the term $-\nabla p$ in equation (5) becomes $-c^2 \nabla \rho$. The equations actually solved by the finite difference scheme are:

$$\partial_t \boldsymbol{v} + (\boldsymbol{v} \cdot \nabla)\boldsymbol{v} + 2(\hat{\boldsymbol{x}} + \Omega_P \boldsymbol{p}(t)) \times \boldsymbol{v} = -c^2 \nabla \rho + \mathrm{Ek} \nabla^2 \boldsymbol{v} + \Omega_P \omega_D (\hat{\boldsymbol{x}} \times \boldsymbol{p}(t)) \times \boldsymbol{r}, \tag{8}$$

$$\partial_t \rho + \nabla \cdot \boldsymbol{v} = 0. \tag{9}$$

The sound speed c is chosen to keep the Mach number $|\boldsymbol{v}|/c$ below 0.04 everywhere. In addition, c needs to be large enough so that the time it takes sound waves to travel across the cube is much less than the rotation period, which expressed in the non-dimensional quantities requires $c \gg 2\pi$. In the simulations presented here, $c^2 = 500$. The simulations are started from $\rho = 1$ and $|\rho - 1|$ stays below 5×10^{-4} during the course of the computations.

For the kinematic dynamo problem, the equations of motion are augmented with the induction equation for the magnetic field $\boldsymbol{B}(\boldsymbol{r}, t)$

$$\partial_t \boldsymbol{B} + \nabla \times (\boldsymbol{B} \times \boldsymbol{v}) = \frac{\mathrm{Ek}}{\mathrm{Pm}} \nabla^2 \boldsymbol{B} \quad , \quad \nabla \cdot \boldsymbol{B} = 0, \tag{10}$$

where the magnetic Prandtl number Pm is given by $\mathrm{Pm} = \frac{\nu}{\lambda}$ with λ the magnetic diffusivity of the fluid.

The boundary conditions are free slip for the velocity field. The magnetic field is only allowed to have a normal component at the boundaries. The tangential components are forced to zero which implies that the normal derivative of the normal component is zero, too, to keep the magnetic field divergence free. These boundary conditions approximate the vacuum boundary conditions and are frequently called pseudo-vacuum boundaries. It would have been preferable to run the simulations for vacuum outside the cube. However, this leads to non-local boundary conditions and much more time consuming computations. While the choice of the magnetic boundary conditions does have some quantitative influence on the dynamo properties of precession driven flow, this influence is too small to be relevant for the conclusions drawn below. A comparison of different magnetic boundary conditions will be presented for an example in spherical geometry, where different types of boundary conditions are easier to implement.

The time step in these simulations is limited by the CFL-criterion based on the sound speed c and the grid size. The spatial resolution was routinely 128^3 and increased to 256^3 or 512^3 for the Ekman number of 10^{-5}. The angle α was always 60°, so that negative Ω_P correspond to retrograde precession. The Ekman numbers varied from 10^{-3} to 10^{-5}. The second control parameter, $\Omega = \Omega_P/\omega_D$ was varied from -0.26 to 0. The simulations focused on negative Ω since in previous studies, retrograde precession was found to be less stable [19, 20].

3. Hydrodynamics

The small amplitude response to weak precession in spheres and ellipsoids which can be described by the linearized equations of motion is a particular inertial mode, the spin-over mode, which corresponds to a rotation of the fluid about an axis different from the rotation axis of the container. For arbitrary precession in these geometries, we even have an analytical solution for the full equation of motion including the nonlinear terms for an ideal fluid, the so called Poincaré solution. This is a motion with spatially uniform vorticity. At finite viscosity, we also have an analytical prediction for this vorticity, valid for small Ekman numbers and precession rates [21], which is largely confirmed by numerical simulations [19, 22]. In analogy with studies in spheroidal geometry, we consider the energy density of the flow in the frame of the boundaries: $E_{\mathrm{kin}} = \frac{1}{V}\langle \int \frac{1}{2} \boldsymbol{v}^2 \mathrm{d}V \rangle$, where $\langle ... \rangle$ denotes average over time and the integration extends over the entire fluid volume V. The division by V is in fact immaterial here because the cube has unit volume. The rotation of the fluid is best represented in the precession frame, because it shows the more intuitive behavior in this frame: for zero precession, the fluid rotates about the same axis as the container, but the fluid axis departs from the container axis as precession is increased. In order to pursue the analogy with spheres, it is useful to compute the vorticity of the fluid $\boldsymbol{\omega}$ averaged over spherical shells centered at the center of the cube:

$$\boldsymbol{\omega}(r) = \frac{1}{V'} \left\langle \int \frac{1}{2} \nabla \times \boldsymbol{v} \mathrm{d}V' \right\rangle + \omega_D \hat{\boldsymbol{x}}, \tag{11}$$

where V' is the volume of the intersection of the shell of radius r (and thickness 1/128 in the figures below) and the cube. The addition of $\omega_D \hat{\boldsymbol{x}}$ transforms the rotation in the boundary frame into rotation in the precession frame.

For several visualizations below, it will be necessary to obtain rotation axis for the fluid as a whole. We compute an average rotation $\boldsymbol{\omega}_F$ as

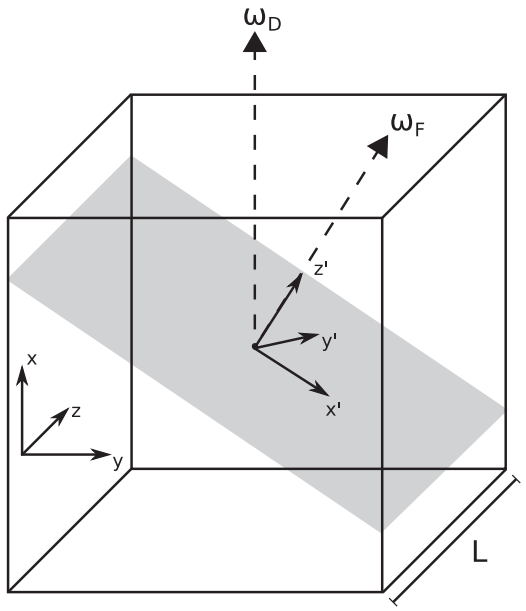

Figure 1. Sketch of the system and two frames of reference: the tripod (x, y, z) is fixed with respect to the boundaries, with x pointing along ω_D. The tripod (x', y', z') moves relative to (x, y, z) such that z' always points along ω_F.

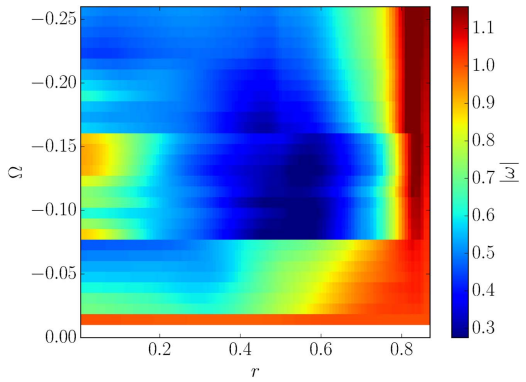

Figure 2. Contour plot of $|\omega|$ in the (Ω, r)-plane for $\mathrm{Ek} = 2.5 \times 10^{-4}$.

$$\omega_F = \frac{3}{4\pi\Delta r^3}\int_0^{\Delta r} \omega(r) 4\pi r^2 \mathrm{d}r. \tag{12}$$

It is certainly useful to spare out the corners of the cube in this average. The average is calculated with $\Delta r = 0.1$ in the upcoming figures which visualize flow structures in the equatorial plane perpendicular to the fluid axis (the shaded plane in figure 1).

The time average in equation (11) is necessary even for laminar flows. The cube rotates within the precession frame so that a vorticity which is a constant vector in this frame forms different angles with the edges of the cube as time goes on. The interaction between the fluid and the boundaries certainly depends on the orientation of the fluid rotation axis within the cube, and we expect that the rotation of the fluid is never time independent.

The interaction with corners also leads to sudden variations of the rotation profile $\omega(r)$ as Ω is varied. This is best seen on contour plots of $|\omega|$ in the (Ω, r)-plane as the example in figure 2 for $\mathrm{Ek} = 2.5 \times 10^{-4}$. There are two apparent discontinuities, at $\Omega \approx -0.075$ and $\Omega \approx -0.16$. For $-0.075 > \Omega > -0.16$, there is a local maximum of $|\omega(r)|$ at $r = 0$, and the minimum near $r = 0.5$ is lower than at other Ω. Similar transitions are observed at different Ek, but the $|\Omega|$ at which the transitions occur decrease with decreasing Ek. The radius to the closest boundary is 0.5, which is the radius of the largest sphere enclosed by the cube. The variations of $\omega(r)$ found in the cube are generally larger than the variations seen in the sphere at comparable parameters.

A convenient summary of the discontinuous behavior of the global rotation is given by the angle θ_F between the axes of the fluid and the container, computed from $\omega_F \cdot \hat{\boldsymbol{x}} = |\omega_F| \cos\theta_F$. This angle is plotted in figure 3. The discontinuities observed in the contour plot of $|\omega|$ (figure 2) are found again in figure 3.

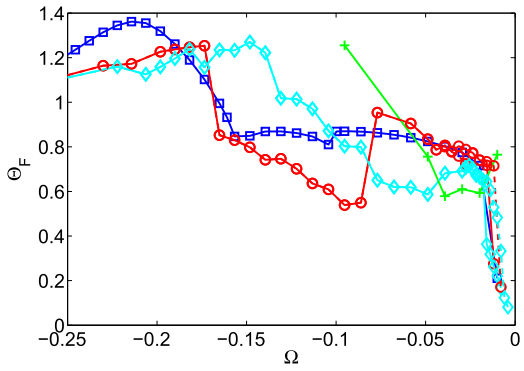

Figure 3. θ_F as a function of Ω for Ek $= 10^{-3}$ (squares), 2.5×10^{-4} (circles), 10^{-4} (diamonds) and 10^{-5} (crosses). Hysteresis loops are indicated by dashed lines. The dashed branch is obtained by decreasing |Ω| and going from left to right in the figure, the continuous line is obtained by going in the opposite direction.

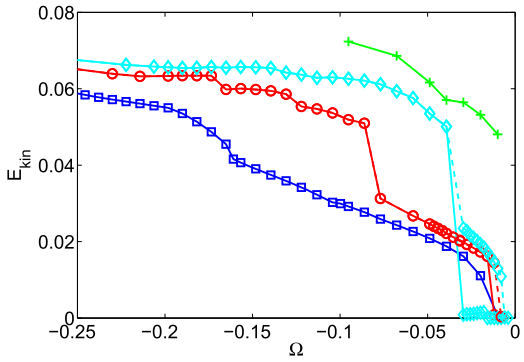

Figure 4. $E_{\rm kin}$ as a function of Ω for Ek $= 10^{-3}$ (squares), 2.5×10^{-4} (circles), 10^{-4} (diamonds) and 10^{-5} (crosses). Hysteresis loops are indicated by dashed lines. The dashed branch is obtained by decreasing |Ω| and going from left to right in the figure, the continuous line is obtained by going in the opposite direction.

The kinetic energy $E_{\rm kin}$ is shown for retrograde precession in figure 4. It has the general behavior well known from spheres and spheroids, meaning that $E_{\rm kin}$ increases with increasing precession rate. However, there are some conspicuous jumps in the curves in figure 4. These are related to the discontinuities already observed in $|\boldsymbol{\omega}(r)|$ and θ_F. Furthermore, the behavior is hysteretic and $E_{\rm kin}$ depends on whether a given precession rate was reached by increasing the precession rate from a previous, lower value, or if on the contrary the simulation was started from a state obtained at larger precession rate. These hysteresis loops suggest that the fluid's rotation axis is pinned in certain positions relative to the edges of the cube. Hysteresis loops in $E_{\rm kin}$ correlate with hysteresis loops in in θ_F. Note that the discontinuities at $\Omega < -0.07$ show no hysteresis, neither in $E_{\rm kin}$ nor in θ_F.

Sudden reorientations of the fluid axis are also known from spheroids. In this case, they are due to two possible equilibria between viscous and pressure torques [9, 23]. This mechanism is presumably unrelated to what we observe in the cube, because at fixed *Ek*, there is more than one Ω at which a reorientation occurs in the cube (and only one in the ellipsoid) and these Ω are much smaller in absolute value than the corresponding value in ellipsoids of small ellipticity, and there is no such Ω at all in a sphere.

We next turn to instabilities. Following previous studies [19], it is convenient to consider the energy $E_{\rm a}$ contained in the flow components $\boldsymbol{v}_{\rm a}$ antisymmetric with respect to inversion at the center of the cube:

$$\boldsymbol{v}_{\rm a} = \frac{1}{2}(\boldsymbol{v}(\boldsymbol{r}) + \boldsymbol{v}(-\boldsymbol{r})), \quad E_{\rm a} = \frac{1}{V}\left\langle \int \frac{1}{2}\boldsymbol{v}_{\rm a}^2 \mathrm{d}V \right\rangle. \tag{13}$$

The inhomogeneous term in equation (5) has the wrong symmetry to directly force a flow with $E_{\rm a} \neq 0$. It is only possible to find $E_{\rm a} \neq 0$ with an intervening instability. On the other hand, the laminar flow can become unstable to a disturbance which has the same symmetry as the spin-over mode so that $E_{\rm a}$ stays zero despite an instability [24]. But $E_{\rm a} \neq 0$ is a sure sign of an instability.

$E_{\rm a}/E_{\rm kin}$ is shown as a function of Ω for different Ek in figure 5. There can of course be no instability for $\Omega = 0$. As the retrograde precession is increased, one finds instabilities, possibly separated by intervals with $E_{\rm a} = 0$. This picture is again familiar from triad resonances found in spheres and ellipsoids. A triad resonance

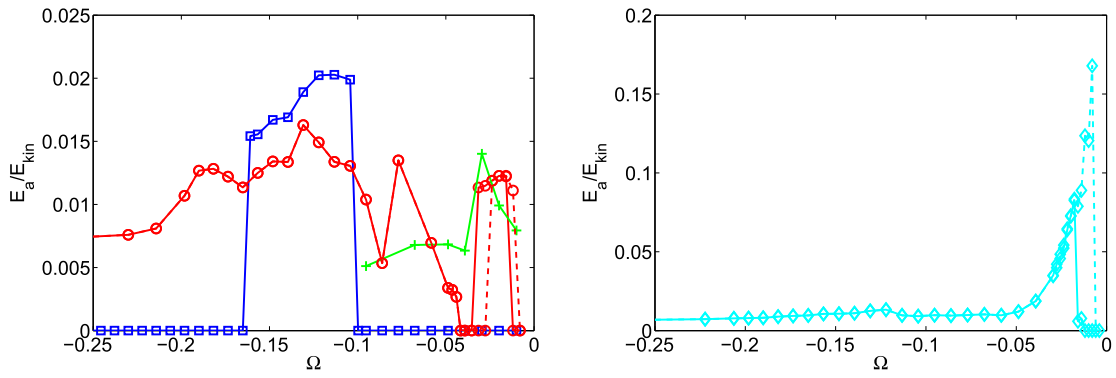

Figure 5. E_a/E_{kin} as a function of Ω for Ek $= 10^{-3}$ (squares), 2.5×10^{-4} (circles), 10^{-4} (diamonds) and 10^{-5} (crosses). The graph is split into two panels for better readability. The right panel shows the curve for Ek $= 10^{-4}$ which leads to the largest values of E_a/E_{kin}. Hysteresis loops are indicated by dashed lines. The dashed branch is obtained by decreasing $|\Omega|$ and going from left to right in the figure, the continuous line is obtained by going in the opposite direction.

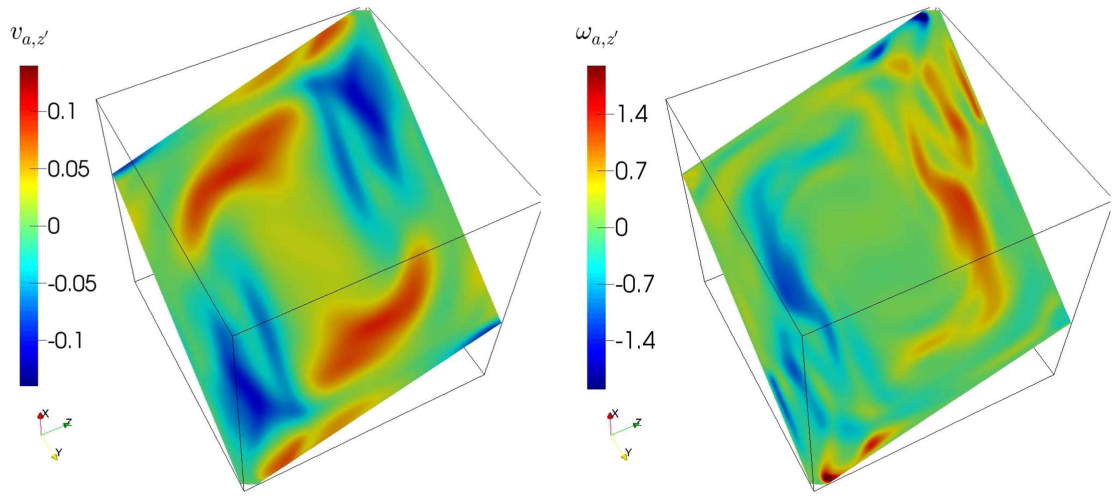

Figure 6. Visualization of the components parallel to the rotation axis of the fluid of antisymmetric velocity (left panel) and antisymmetric vorticity (right panel) in the plane perpendicular to the rotation axis of the fluid for Ek $= 10^{-4}$, $\Omega = -0.02$.

occurs if two inertial modes are coupled by the laminar stable flow, which is counted as third mode of the triad. The inertial modes are viewed as solutions of the unperturbed, non-precessing flow, and the coupling appears in a perturbation calculation which treats the precession rate as a small parameter. In order to obtain a triad resonance with an energy growing in time, the inertial modes in the triad need to satisfy certain selection rules, for instance concerning the azimuthal wavenumbers [25].

For flows close to the onset of instability, the modes involved in the triad can be identified visually. Further away from the onset, the flow becomes chaotic and inertial modes cannot be readily recognized within the turbulence. In order to find triads, the most convenient procedure is the one used in [2, 20]: first change to a frame of reference (x', y', z') in which the fluid axis defined by equation (12) points along z'. Then select the 'equatorial' plane perpendicular to the z′-axis containing the center of the cube (see figure 1). Plots of $v_{az'} = \boldsymbol{v}_a \cdot \hat{\boldsymbol{z}}'$ and $\omega_{az'} = \frac{1}{2}((\nabla \times \boldsymbol{v})(\boldsymbol{r}) + (\nabla \times \boldsymbol{v})(-\boldsymbol{r})) \cdot \hat{\boldsymbol{z}}'$ in this equatorial plane will reveal modes in a triad if they are excited by laminar flows with corrections to the spin-over mode of azimuthal wavenumber 1. Figures 6 and 7 show pairs of modes with azimuthal wavenumbers 4 and 5 in figure 7 and 1 and 2 in figure 6 which fulfill the condition that the wavenumbers differ by 1. If such pairs of modes appeared near the onset of instability, they were always combinations of wavenumbers 4 and 5 or 1 and 2 in the present simulations. At parameters away from the stability limit, the flow becomes increasingly disordered, even if hints of underlying inertial modes may still be discerned (figure 8).

No analytical solution exists for inertial modes in cubes [26], and we did not compute them numerically. Strictly speaking, we have not proven that figures 6–8 show inertial modes, and even less that they form a triad because this requires a certain interaction integral to be different from zero which we did not check. However,

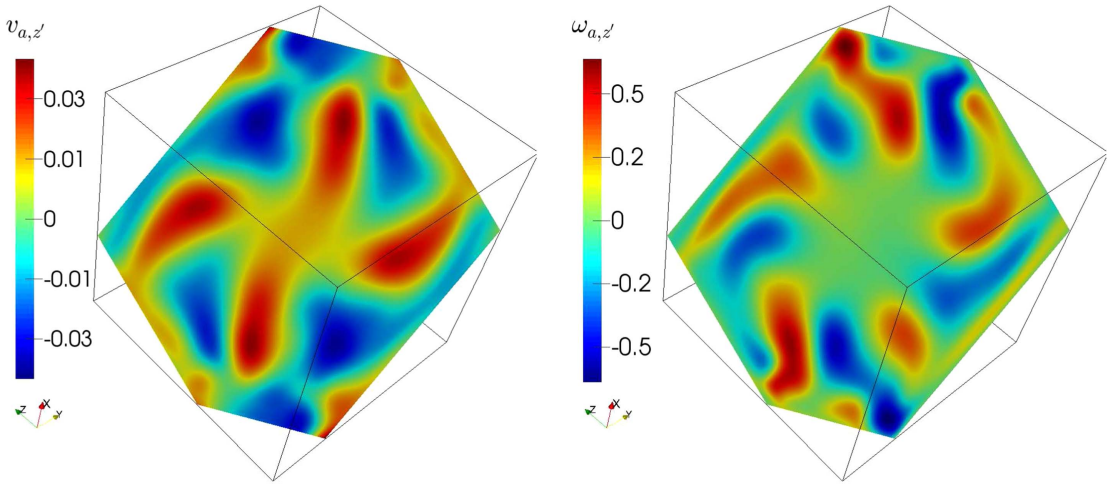

Figure 7. Visualization of the components parallel to the rotation axis of the fluid of antisymmetric velocity (left panel) and antisymmetric vorticity (right panel) in the plane perpendicular to the rotation axis of the fluid for Ek $= 2.5 \times 10^{-5}$, $\Omega = -0.02$.

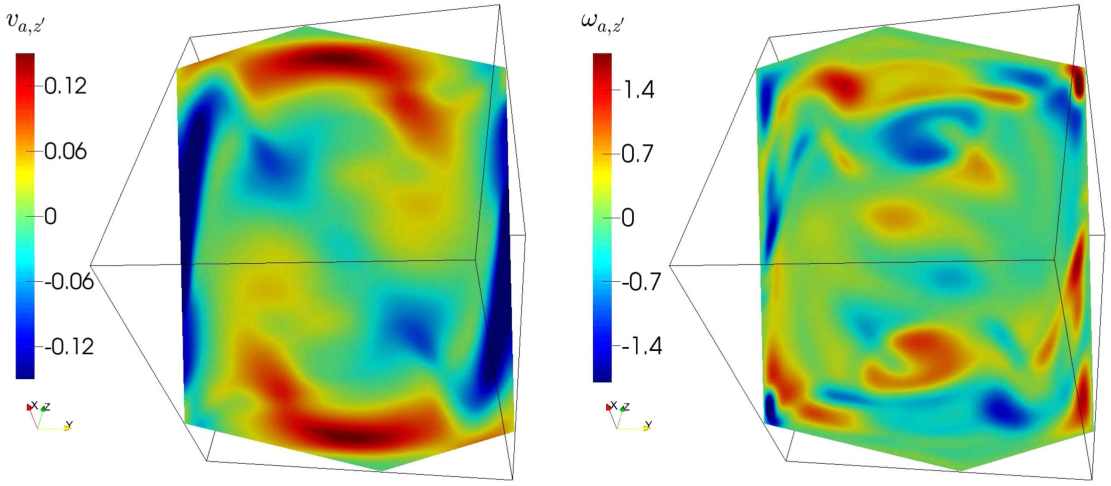

Figure 8. Visualization of the components parallel to the rotation axis of the fluid of antisymmetric velocity (left panel) and antisymmetric vorticity (right panel) in the plane perpendicular to the rotation axis of the fluid for Ek $= 2.5 \times 10^{-5}$, $\Omega = -0.14$.

the similarity of figures 6–8 with analogous figures for spheres is compelling, so that there can be little doubt that the same triad resonance mechanism is at work in both cubes and spheres.

It is revealing to look at the spatial distribution of antisymmetric energy because it varies with Ω. Let us define a radial distribution ϵ_a by averaging E_a over spherical shells in the same way as was done for $\boldsymbol{\omega}$ in equation (11):

$$\epsilon_a(r) = \frac{1}{V'}\left\langle \int E_a \, \mathrm{d}V' \right\rangle. \tag{14}$$

Figure 9 shows a contour map of ϵ_a in the (Ω, r)-plane at the same Ek as figure 2. Depending on Ω, there is a local maximum of ϵ_a near $r = 0$, near $r = 0.7$, or near both. The eddies visible in figures 6–8 explain the maximum near $r = 0.7$, but it is more surprising to also find a maximum near the origin for some parameters.

A point of view complementary to figure 5 is to study E_a/E_{kin} as a function of Ek at fixed Ω, as in figure 10. It is clear that for $Ek \to \infty$, all instabilities have to disappear and E_a is zero. It is therefore not surprising to see E_a/E_{kin} rise in figure 10 as Ek is decreased starting from large values. Perhaps more surprisingly, there is an Ek at which E_a/E_{kin} reaches a maximum for Ω fixed, and E_a/E_{kin} decreases with decreasing Ek at small Ek. In order to trigger an instability, the basic flow needs to be different from a pure solid body rotation. The profile of $|\boldsymbol{\omega}(r)|$ and hence deviations from solid body rotation, depends in a complicated way on Ω and Ek because of the corners of the cube, as exemplified in figure 2. A simplification of the hydrodynamic behavior in general and of E_a/E_{kin} in particular is expected if deviations from solid body rotation are not only induced by corners. In an ellipsoid for instance, the Poincaré flow of inviscid fluid contains shear related to the ellipticity of the container

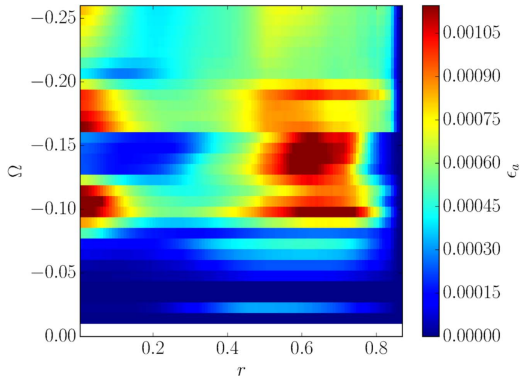

Figure 9. Contour plot of ϵ_a in the (Ω, r)-plane for $\mathrm{Ek} = 2.5 \times 10^{-4}$.

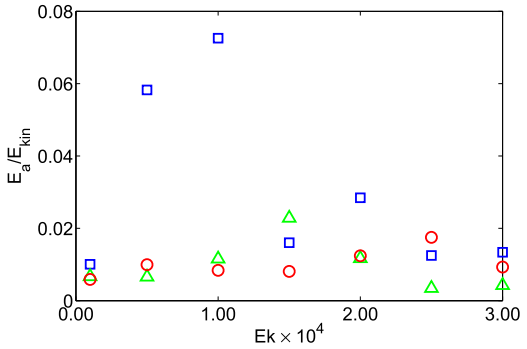

Figure 10. E_a/E_{kin} as a function of Ek for $\Omega = -0.02$ (squares), -0.05 (triangles) and -0.1 (circles).

[25], in absence of any corners. The best Cartesian approximation to an ellipsoid is a cuboid. These considerations led us to perform a few simulations in a cuboid with side lengths in the ratio 1:1:1.85. And indeed, we found E_a/E_{kin} to reach a plateau without noticeable variation below a certain Ek. This finding confirms that the behavior in figure 10 is specific to a cube and does not exist in a general cuboid. We now also expect to find the same behavior in spheres, where it has not been reported up to now, possibly because simulations never used small enough Ekman numbers and sufficiently large Ω.

With the aim of building a precession driven dynamo experiment in mind, it is of interest to find geometries which divert as much energy as possible from the basic Poincaré flow, which is toroidal and ineffective as a dynamo, into more complicated flow. E_a/E_{kin} therefore serves as a figure of merit, because a larger E_a/E_{kin} guarantees that a larger fraction of energy is in the antisymmetric modes which cannot be part of laminar precession driven flow. One motivation to study cubes instead of spheres is that one expects E_a/E_{kin} to be generally larger in the cube. At equal average vorticity of the interior flow, the flow either flows over smooth boundaries in a sphere, or passes the edges and corners of a cube. One expects the latter case to stir the fluid more efficiently because of a stronger coupling between the boundaries and the fluid, and one expects larger E_a/E_{kin} in the cube.

When comparing the results for the cube with those obtained for spheres in [1, 2], one has to keep in mind that the Ekman and Reynolds numbers in those references are based on radius instead of diameter. For the purpose of comparison, these Ekman and Reynolds numbers have to be divided by 4 and multiplied by 2, respectively.

The expectation of a larger E_a/E_{kin} in the cube is roughly fulfilled. For instance, in a sphere at $\mathrm{Ek} = 1.25 \times 10^{-4}$ with $\alpha = 60°$, E_a/E_{kin} is less than 6×10^{-3} at all Ω [1]. In the cube at $\mathrm{Ek} = 10^{-4}$, $E_a/E_{kin} > 6 \times 10^{-3}$ for $-0.24 < \Omega < -0.006$ with a maximum at $\Omega = -0.008$ which lies on the branch of a hysteresis loop obtained when decreasing $|\Omega|$ (figure 5). However, the instability occurs through a triad resonance and eigenfrequencies depend on container shape, so that one can also find counter examples of the sort that at some Ω, one hits a resonance in the sphere which becomes unstable, but the cube is stable at the same Ω, so that E_a/E_{kin} is larger in the sphere than in the cube at some Ω. This happens for example at $\Omega = -0.3$ and $\mathrm{Ek} = 0.75 \times 10^{-4}$.

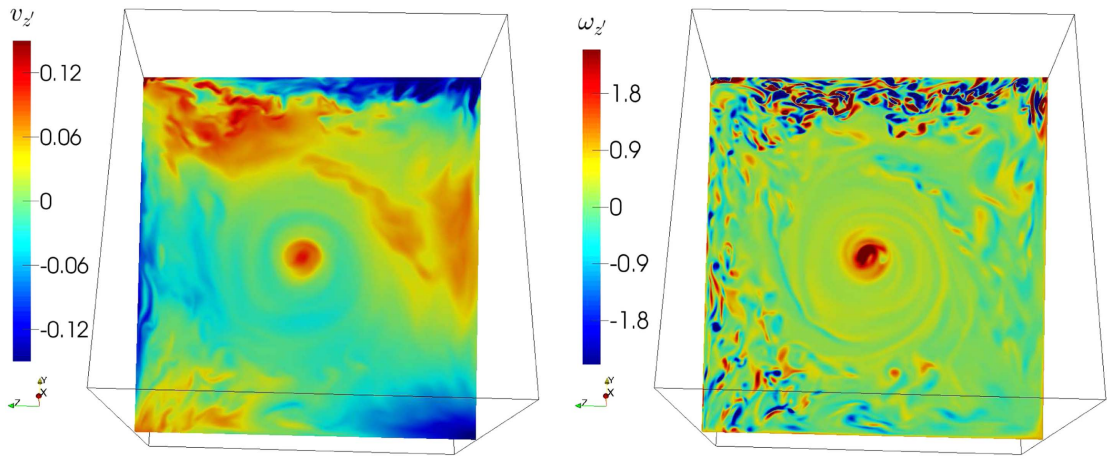

Figure 11. Visualization of the components parallel to the rotation axis of the fluid of total velocity (left panel) and total vorticity (right panel) in the plane perpendicular to the rotation axis of the fluid for $\mathrm{Ek} = 10^{-5}$, $\Omega = -0.02$. Note that figures 6–8 show antisymmetric, not total velocity or vorticity.

When applying the results of numerical simulations to laboratory experiments or astrophysical objects, it is always necessary to extrapolate results to smaller Ek. This turns out to be difficult in the cube, even in hydrodynamics without magnetic fields. The reason is that at constant Ω, flow patterns may change qualitatively as Ek tends to zero. The best example is $\Omega = -0.02$. At $\mathrm{Ek} = 2.5 \times 10^{-4}$, one observes two modes with $m = 4$ and 5 (figure 7). At $\mathrm{Ek} = 2 \times 10^{-4}$, these two modes have disappeared and are replaced by two other modes with $m = 1$ and 2. Decreasing Ek further, one suddenly finds at $\mathrm{Ek} = 10^{-5}$ a flow consisting of a single cyclonic vortex, which decays typically every 4 to 5 rotations into small scale turbulence before reforming again within less than a single rotation period (figure 11). Such a single vortex state is also observed at $\mathrm{Ek} = 10^{-5}$ at the neighboring precession rates of $\Omega = -0.01$ and -0.03, but not at -0.04 and beyond.

The single vortex state reminds of observations made in cylinders [27] and spheres [28] of a few vortices forming and steadily drifting. What sets the cube apart is that the reorganization of the small scale turbulence is so complete that only a single vortex is left over.

The mechanism responsible for the formation of this vortex remains to be elucidated. An inverse cascade is a natural candidate. But it should be noted that already at less extreme parameters, increased cyclonic vorticity appears at the origin, as for instance at $\mathrm{Ek} = 2.5 \times 10^{-5}$ near $\Omega = -0.14$ as shown in figure 2.

4. Kinematic dynamos

The induction equation (10) is now solved together with the equations of motion to investigate the generation of magnetic fields. The back reaction of the magnetic field on the flow is not included so that there will not be any information about the saturation field strength. If magnetic fields grow from a seed field, they will do so exponentially in a time independent flow. If the flow is turbulent and statistically stationary, the time evolution of the magnetic field over long times can still be fitted to an exponential. The growth rate deduced from such a fit is determined for different Pm. Of particular interest is the critical magnetic Prandtl number, Pm_c, above which magnetic fields grow whereas they decay for $\mathrm{Pm} < \mathrm{Pm}_c$.

We tried to reproduce the results of [10] who studied a precessing cube with perfectly conducting boundaries. It was a simple matter to implement these boundary conditions instead of the pseudo-vacuum boundaries, but we did not use the same initial conditions to start the simulations. At any rate, we could not find any growing magnetic fields for the control parameters given in [10] and assume that these simulations simply were not run for long enough. The graphs shown in that paper cover intervals of time shorter than the transients in our simulations. Transient growth of course did occur, but eventually, all fields decayed.

Dynamos have been found only in flows with $E_a \neq 0$, at least for $\mathrm{Pm} \leqslant 11$. This implies that a hydrodynamic instability is necessary. A selection of critical Pm is shown in figure 12. The smallest Pm_c is 0.24 and corresponds to the flow with a single vortex (figure 11). Flows without a single vortex at the same Ek have a Pm_c larger by at least 30%. In figure 12, there is a general trend for Pm_c to decrease with decreasing Ek. This suggests that critical magnetic Reynolds numbers may asymptote towards constants at small Ek and motivates us to investigate magnetic Reynolds numbers.

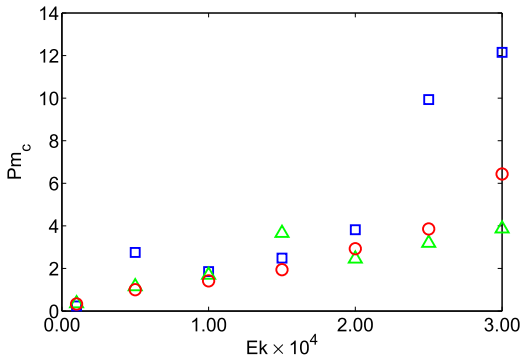

Figure 12. $\mathrm{Pm_c}$ as a function of Ek for $\Omega = -0.02$ (squares), -0.05 (triangles) and -0.1 (circles).

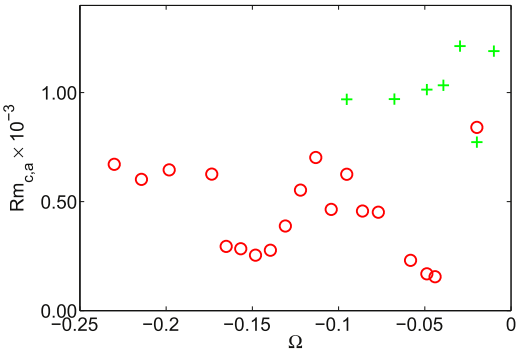

Figure 13. $\mathrm{Rm_{c,a}}$ as a function of Ω for $\mathrm{Ek} = 2.5 \times 10^{-4}$ (circles) and 10^{-5} (crosses).

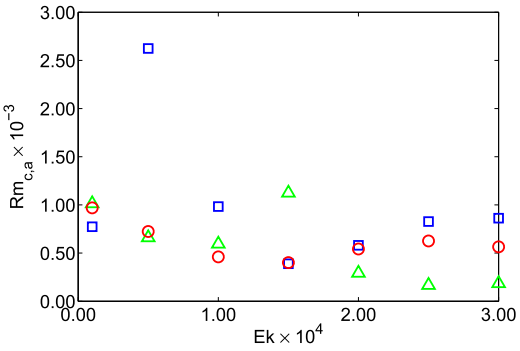

Figure 14. $\mathrm{Rm_{c,a}}$ as a function of Ek for $\Omega = -0.02$ (squares), -0.05 (triangles) and -0.1 (circles).

There are several potentially useful definitions of magnetic Reynolds number. First, there is the critical magnetic Reynolds number based on E_a, defined as

$$\mathrm{Rm_{c,a}} = \sqrt{2E_a}\,\mathrm{Pm_c}/\mathrm{Ek}.$$

This definition is motivated from the observation that the total kinetic energy includes the basic solid body rotation of the spin-over mode which is not useful for the dynamo, whereas E_a measures only motion which is essential to the dynamo. E_a is not modified upon changing between the boundary frame, the precession frame, and the inertial frame. $\mathrm{Rm_{c,a}}$ puts a number on whether the flow excited by instability is an efficient dynamo or not.

$\mathrm{Rm_{c,a}}$ is shown in figures 13 and 14 as a function of Ω and Ek. The smallest value in this collection is 155 (obtained for $\mathrm{Ek} = 2.5 \times 10^{-4}$ and $\Omega = -0.044$). The other critical magnetic Reynolds numbers are between 155 and 3000. For comparison, the lowest value known for a precessing spherical dynamo is approximately 400 (based on the diameter of the sphere), which is found for $\mathrm{Ek} = 1.25 \times 10^{-4}$ (again based on the diameter of the

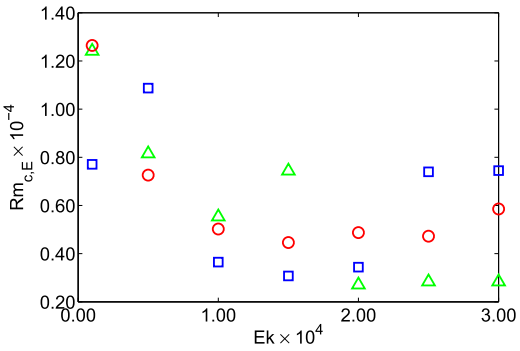

Figure 15. $Rm_{c,E}$ as a function of Ek for $\Omega = -0.02$ (squares), -0.05 (triangles) and -0.1 (circles).

sphere), $\alpha = 60^\circ$ and $\Omega = -0.3$ [1], whereas $Rm_{c,a} = 1280$ for $\Omega = -0.14$ [2]. Using $Rm_{c,a}$ as figure of merit, the dynamos in precessing cubes are better than dynamos in spheres by a factor of more than 2. It is not clear where this improvement comes from, considering the similarity of the flows in the two geometries.

In figure 13, $Rm_{c,a}$ has two minima as a function of Ω for $Ek = 2.5 \times 10^{-4}$. A well defined triad dominates the flow around $\Omega = -0.05$, whereas the flow is more chaotic and is dominated by different azimuthal wavenumbers for $\Omega = -0.11$ and contains again a recognizable triad at $\Omega = -0.15$. In addition, the radial variation of rotation is different at both Ω (figure 2), which leads to different ω-effects in the parlance of mean field magnetohydrodynamics. It is not surprising that different combinations of inertial modes and differential rotation lead to more or less efficient dynamos, even though it requires detailed numerical computation to tell which combination is optimal.

The single vortex flow of figure 11 is also a dynamo, with $Rm_{c,a} = 824$. This is however not a very relevant number, because the flow in the vortex has the wrong symmetry to contribute to E_a. Also, $Rm_{c,a}$ is not a number directly useful for the design of laboratory experiments, which are limited among others by the power delivered by the motors driving the experiment. Let us therefore consider the critical magnetic Reynolds number based on E_{kin}, defined as

$$Rm_{c,E} = Rm_{c,a}\sqrt{E_{kin}/E_a}.$$

If $E_{kin} = 0$, there is no motion of the fluid relative to the boundaries and no dissipation. The dissipation will increase with E_{kin}, even though the exact functional dependence is not known. If one designs an experiment, one certainly wants to minimize $Rm_{c,E}$. One can hope that the cube further improves upon the sphere by this measure because of the larger E_a/E_{kin} found at most parameters. Disappointingly, figure 15 shows that this is not the case, because for the dynamos with a small $Rm_{c,a}$, E_a/E_{kin} is actually relatively small. The smallest $Rm_{c,E}$ found in the cube is approximately 2800. The two spherical dynamos cited in the previous paragraph have $Rm_{c,E} = 4560$ (for $\Omega = -0.3$) and $Rm_{c,E} = 16500$ (for $\Omega = -0.14$).

Another experimental limit is the rotation rate that can be imparted to the container, best quantified as the magnetic Reynolds number based on the rotation speed, Rm_{rot}, which is given by

$$Rm_{rot} = Pm/(2Ek).$$

The design for the experiment in Dresden [12, 13] for instance is limited to $Rm_{rot} < 1420$. The values found for the critical Rm_{rot} in the simulations exceed this limit by more than a factor of 2 (figure 16). The smallest simulated Rm_{rot} is around 3200. From figure 17, one cannot expect that this number will be much reduced in going from the simulated Ekman numbers of 10^{-5} and larger to the Ekman numbers of the experiment of 10^{-8}.

In figures 14–17, the magnetic Reynolds number seems to generally increase with decreasing Ekman number for Ek below 10^{-4}. With the units chosen in this paper, velocities are given in multiples of the global rotation speed, so that the adimensional velocity is directly a Rossby number. This number is less than 1 in all simulations presented here and there is no systematic dependence of the magnetic Reynolds numbers on the Rossby number. It is thus impossible to detect any effect of a rotational constraint on the flow. But decreasing Ek also broadens the spatial spectrum of the turbulent fluctuations and adds small scales to the flow. The increase of the magnetic Reynolds numbers at small Ek indicates that these small scales increase the magnetic eddy diffusivity without increasing in the same proportion the induction and magnetic field generation.

Extrapolations to small Ekman numbers are uncertain due to the hydrodynamic transitions described in the previous section, in particular the appearance of a flow consisting of a single vortex. It is not yet known whether such a state will arise for all precession rates for small enough Ek. Among the examples of single vortex flows we know, the smallest magnetic Reynolds numbers are $Rm_{c,E} = 7700$ and $Rm_{rot} = 1.2 \times 10^4$.

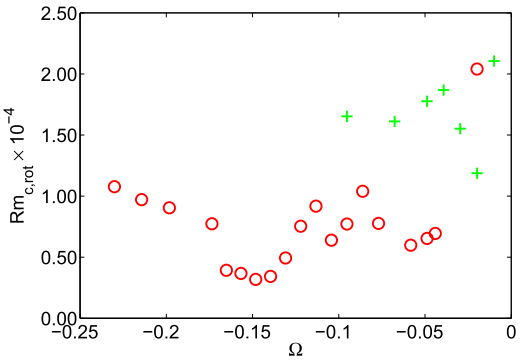

Figure 16. $\mathrm{Rm}_{\mathrm{c,rot}}$ as a function of Ω for $\mathrm{Ek} = 2.5 \times 10^{-4}$ (circles)and 10^{-5} (crosses).

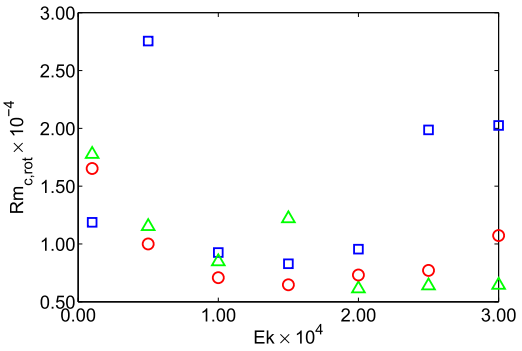

Figure 17. The critical $\mathrm{Rm}_{\mathrm{rot}}$ as a function of Ek for $\Omega = -0.02$ (squares), -0.05 (triangles) and -0.1 (circles).

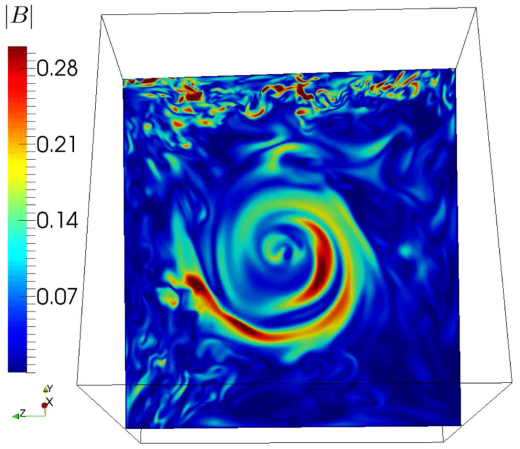

Figure 18. Visualization of the magnitude of the magnetic field in the plane perpendicular to the rotation axis of the fluid for $\mathrm{Ek} = 10^{-5}$, $\Omega = -0.02$.

The magnetic field generated by the vortex reflects the underlying flow in that the field is wrapped around the vortex (figure 18). In the other flows, plots of magnetic field intensity reveal large amplitudes along the perimeter of the flow with little signature of the structures of the modes in the triad resonance (figure 19). This is mostly due to the fact that these modes are part of the antisymmetric motion, which makes up a small fraction of the total energy. The symmetric motion on the other hand is mostly a rotation with dead water in the corners and shear zones surrounding the core of the flow which stretch the magnetic field and lead to the large amplitudes seen in figure 19.

The boundary conditions implemented in our simulations are not a perfect representation of an experiment. However, the simplification of boundary conditions has no dramatic impact on critical Reynolds numbers in

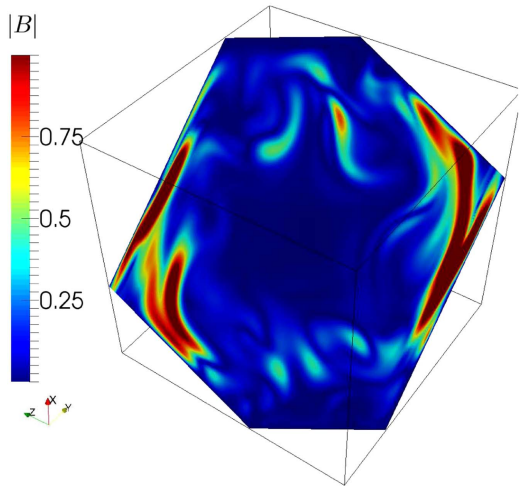

Figure 19. Visualization of the magnitude of the magnetic field in the plane perpendicular to the rotation axis of the fluid for $\mathrm{Ek} = 2,\ 5 \times 10^{-4},\ \Omega = -0.02$.

precessing flows, presumably because of the large shear between the boundary layers and the Poincaré flow in the interior. Shear occurs in boundary layers in precessing spheres with no slip boundaries, and the magnetic field amplitudes at the perimeter of the core visible in figure 19 are also indicative of shear. To test the effect of boundary conditions for the magnetic field, we simulated dynamos in precessing spheres for three different boundary conditions with minor modifications of the code of [1]: (1) vacuum outside the sphere, (2) pseudo-vacuum conditions (normal derivative of normal component and tangential components of $\boldsymbol{B}$ are zero) and (3) perfect conductor outside the sphere (normal component and normal derivatives of tangential components of $\boldsymbol{B}$ are zero). The example chosen for this comparison is one of the dynamos in figure 2 of [1] at $\mathrm{Ek} = 0.75 \times 10^{-4}$ (Ek being computed with the diameter of the sphere) and $\Omega = -0.3,\ \alpha = 60°$. The critical Pm for vacuum and pseudo-vacuum boundaries are within 1% of each other, whereas the $\mathrm{Pm_c}$ for a perfect conductor outside the sphere is 20% below the $\mathrm{Pm_c}$ for vacuum boundary conditions. Among the three standard magnetic boundary conditions, the perfectly conducting boundaries lead to the smallest critical magnetic Reynolds numbers.

5. Conclusions

Fluid instabilities in precessing cubes and spheres share similarities which take root in similar laminar basic flows. In a sphere, this is a simple solid body rotation modified by viscous effects at the boundaries. In a cube, the basic flow is still mainly a rotation, modified by the presence of corners. The instability, detected by the energy E_a of the antisymmetric modes, proceeds through a triad resonance. This phenomenon is well studied in spheres [2, 28], and the main features of this mechanism reappear in the cube. In the present study, E_a is a function of two control parameters, Ω and Ek. Close to the line $E_a = 0$ in this 2D parameter space, it is possible to identify triads as in figures 6 and 7, which dissolve further away from the onset of instability into turbulent or chaotic flow. At the smallest Ek simulated so far, the flow can become simple again by forming a single vortex which every time and again decays into small scale structures before reassembling again.

Kinematic dynamos are found among the flows with $E_a \neq 0$ with magnetic Reynolds numbers of the same order of magnitude as in spheres, irrespective of how these numbers are defined. Nonetheless, the minimal magnetic Reynolds numbers in the cube are about a factor of 2 smaller than those known for the sphere. The magnetic Reynolds number can be based on three different velocities: the typical velocity of antisymmetric components, the total velocity relative to the container, and the rotation velocity of the container. The first of these tells us whether the velocity profile in antisymmetric modes could be optimized in order to reduce the critical magnetic Reynolds number. Comparing the numbers found here with those of, for instance, the spherical dynamos in [29], and taking into account that the instabilities also excite symmetric components presumably helpful to the dynamo not accounted for in E_a, we conclude that this critical magnetic Reynolds number cannot be reasonably expected to be much smaller than the numbers computed here. It is in fact surprising that the cube improves upon the sphere by a factor of 2. On the other hand, one might have expected further improvement regarding the other definitions of the Reynolds number, because the corners and edges of the cube act as a surface roughness compared with the sphere and lead to better coupling between fluid and boundary motions. The fluid dynamics globally confirm this expectation, but $\mathrm{Rm_{c,a}}$ is large in the flows with a

large E_a/E_{kin}, so that there is no further significant net reduction of critical magnetic Reynolds number of any definition in going from the sphere to the cube.

The critical magnetic Reynolds numbers are at any rate larger than those accessible experimentally [12, 13]. The magnetic Reynolds number of the global rotation can be on the order of 1000 in experiments, but this in itself is useless because pure rotation cannot lead to dynamo action. Modest precession rates, easily realized in experiments, incline the rotation axis of the fluid with respect to the rotation axis of the container by enough so that roughly half of the Reynolds number of the global rotation is available in the rotation relative to the boundaries. This is still a large magnetic Reynolds number and judiciously shaped containers possibly lead to a dynamo effect even in laminar precession driven flow. In simple geometries such as spheres and cubes, an instability is necessary to create flow structures helpful for magnetic field generation. In the examples simulated here, the magnetic Reynolds number of the antisymmetric motions (which are an indicator of instability) is always less than 10% of the magnetic Reynolds number of the global rotation. It is the smallness of this ratio which hurts the enterprise of building a precession driven dynamo based on flow instabilities.

Precession driven flow consisting of few vortices has been observed in cylinders and spheres [27, 28, 30]. These flows are without a doubt related to single vortex flows in the cube. The single vortex state is also a dynamo, with critical magnetic Reynolds numbers typical of precession driven flow in general, i.e. of the same order of magnitude as those of flows resulting from triad resonances.

We conclude from this study that the main challenge for building a precession driven dynamo is to find ways of channeling energy from the global rotation into motions helpful to the dynamo. Viscous effects at the boundaries are known to modify the Poincaré flow in spheres in a way which leads to dynamo action [1], albeit at magnetic Reynolds numbers which render this effect irrelevant for both astrophysical and laboratory applications which usually involve very small Ekman numbers. The next option is to generate the flow capable of dynamo action through an instability. If precession driven dynamos exist in celestial bodies, they must operate this way. However, the energy taken from the Poincaré mode is too small to lead to experimentally manageable critical magnetic Reynolds numbers. The situation seems to be similar in cylinders, where the energy outside modes driven directly by precession does not exceed a few percent of the total energy [31]. The most promising route to a laboratory precession dynamo may therefore be the search for container shapes with a laminar mode which is already a dynamo.

We also conclude that cubes and cuboids are convenient geometries for the numerical study of precession driven flows as they allowed us to collect data for a larger sample of control parameters than would have been possible in an axisymmetric geometry in which no slip boundaries are essential. Even though the cube is the simplest and most symmetric Cartesian shape, future work will focus on cuboids since the flow in this geometry promises to be less sensitive to the corners and to allow more reliable extrapolation toward small Ekman numbers.

Acknowledgments

The authors acknowledge support from the Helmholtz-alliance 'Liquid Metal Technologies'.

References

[1] Tilgner A 2005 *Phys. Fluids* **17** 034104
[2] Tilgner A 2007 *Geophys. Astrophys. Fluid Dyn.* **101** 1
[3] Wu C and Roberts P 2009 *Geophys. Astrophys. Fluid Dyn.* **103** 467
[4] Wu C and Roberts P 2008 *Geophys. Astrophys. Fluid Dyn.* **102** 1
[5] Nore C, Léorat J, Guermond J- L and Luddens F 2011 *Phys. Rev.* E **84** 016317
[6] Cébron D and Hollerbach R 2014 *Astrophys. J. Lett.* **789** L25
[7] Wu C- C and Roberts P H 2013 *Geophys. Astrophys. Fluid Dyn.* **107** 20
[8] Wei X, Arlt R and Tilgner A 2014 *Phys. Earth Planet. Inter.* **231** 30
[9] Lorenzani S and Tilgner A 2003 *J. Fluid Mech.* **492** 363
[10] Krauze A 2010 *Magnetohydrodynamics* **46** 271
[11] Gans R 1970 *J. Fluid Mech.* **45** 111
[12] Stefani F, Eckert S, Gerbeth G, Giesecke A, Gundrum T, Steglich C, Weier T and Wustmann B 2012 *Magnetohydrodynamics* **48** 103
[13] Stefani F, Albrecht T, Gerbeth G, Giesecke A, Gundrum T, Herault J, Nore C and Steglich C 2015 *Magnetohydrodynamics* **51** 275
[14] Monchaux R *et al* 2007 *Phys. Rev. Lett.* **98** 044502
[15] Finke K and Tilgner A 2012 *Phys. Rev.* E **86** 016310
[16] Tilgner A 2015 *Treatise on Geophysics* vol 8 ed G Schubert 2nd edn (Amsterdam: Elsevier) pp 183–212
[17] Tilgner A 2012 *Phys. Rev. Lett.* **109** 248501
[18] Tilgner A 2014 *Phys. Rev.* E **90** 013004
[19] Tilgner A and Busse F 2001 *J. Fluid Mech.* **426** 387
[20] Lorenzani S and Tilgner A 2001 *J. Fluid Mech.* **447** 111
[21] Busse F 1968 *J. Fluid Mech.* **33** 739

[22] Tilgner A 1999 *J. Fluid Mech.* **379** 303
[23] Noir J, Cardin P, Jault D and Masson J-P 2003 *Geophys. J. Int.* **154** 407
[24] Hollerbach R, Nore C, Marti P, Vantieghem S, Luddens F and Léorat J 2013 *Phys. Rev.* E **87** 053020
[25] Kerswell R 1993 *Geophys. Astrophys. Fluid Dyn.* **72** 107
[26] Maas L 2003 *Fluid Dyn. Res.* **33** 373
[27] Mouhali W, Lehner T, Léorat J and Vitry R 1693 *Exp. Fluids* **53** 1432
[28] Lin Y, Marti P and Noir J 2015 *Phys. Fluids* **27** 046601
[29] Dudley M and James R 1989 *Proc. R. Soc.* A **425** 407
[30] Lin Y, Marti P, Noir J and Jackson A 2016 *Phys. Fluids* **28** 066601
[31] Giesecke A, Albrecht T, Gundrum T, Herault J and Stefani F 2015 *New J. Phys.* **17** 113044